Coherent change detection under a forest canopy

P. B. Pincus*† and M. Preiss*
* Defence Science & Technology Group, Edinburgh, SA, Australia
† School of Electrical & Electronic Engineering, University of Adelaide, Adelaide, SA, Australia

***Abstract*—The possibility of repeat-pass coherent change detection of the ground in a forest using synthetic aperture radar imaging is investigated. By vertically beamforming multiple across-track channels per pass, the canopy interference can be suppressed. We formulate this as a dual-layer (ground and volume) multichannel coherence estimation problem and derive the beamformer that optimally suppresses the volume component in each pass. Beamformer performance is analysed using the random-volume-over-ground model of forest scattering. It is shown that reasonable volume suppression is achievable with just three channels, and this performance is not overly sensitive to model parameters. We also discuss the trade-off between foliage penetration and change sensitivity for wavelength selection.**

I. Introduction

Coherent change detection (CCD) is an application of airborne or spaceborne synthetic aperture radar (SAR) that resolves subtle changes on the ground [1], [2, ch. 5.5]. By computing the complex correlation coefficient (the complex coherence) between two repeat-pass SAR images as a local average in a sliding window, and taking the magnitude, a change map is generated, with areas of high correlation indicating little change and areas of low correlation indicating substantial change. The method is sensitive to changes in the complex speckle pattern of the ground clutter caused by rearranged scattering elements, as opposed to changes in scattering intensity [3], [4]. In typical operation, high-frequency (e.g. Ku-band (λ~1.8cm) [5]), wideband radar systems generate fine-resolution SAR images of open landscapes for CCD.

We study the possibility of extending the CCD technique to detect ground disturbances on forest-covered terrain. The idea was first proposed by the authors in [6]. The twin difficulties that must be overcome to achieve this are illustrated in Fig. 1: for a given position on the ground, the near-range part of the canopy will act as a lossy propagation medium, attenuating the incident and scattered energy, and the far-range part of the canopy will layover (i.e. project) onto the ground, such that the pixel value at the nominal ground position will actually contain a mixture of ground and canopy scattering.

The propagation problem is overcome simply by selecting an operating wavelength for which the expected foliage attenuation is not too great. Past foliage penetration experiments suggest that L-band (λ~23cm) is the highest suitable frequency [7]. Whilst lower frequencies offer better penetration, we also require high sensitivity to change, for which higher frequencies are intuitively better. Here we use a SAR simulation to show how coherence varies with wavelength, given a fixed resolution.

The layover problem can be overcome by coherently combining multiple 2D SAR images acquired at slightly different grazing angles to produce a new '3D' image that is steered to the ground such that scattering contributions from other heights

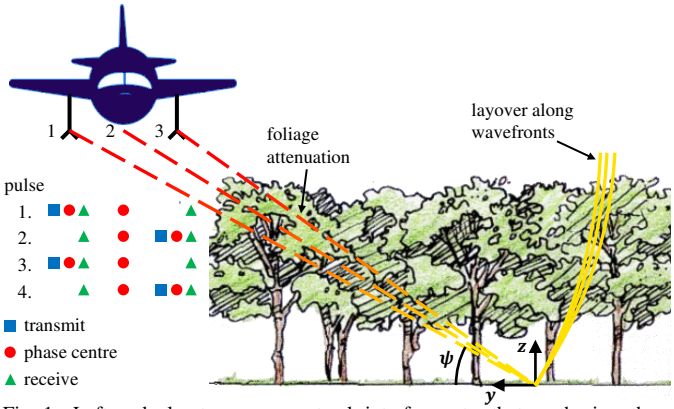

Fig. 1. Left: a dual-antenna, across-track interferometer that synthesises three effective phase centres separated in grazing angle ψ by alternating the transmit antenna pulse-to-pulse and receiving every pulse on both antennas. Right: canopy attenuation and layover.

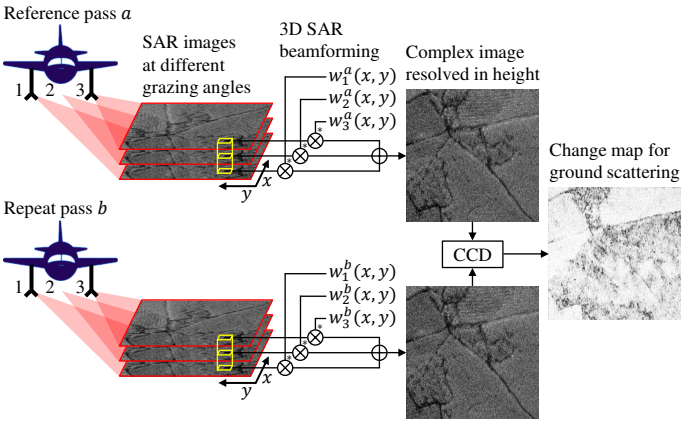

Fig. 2. The proposed 3D SAR CCD concept. SAR images from each pass of a multichannel radar system are vertically beamformed using complex weights $\mathbf{w}=[w_1,w_2,...]^T$, which may vary spatially, to produce a complex '3D' image steered to the ground, with canopy scattering suppressed. The magnitude of the complex coherence between two 3D images indicates change at ground level.

are suppressed. This is 3D SAR beamforming (a.k.a. SAR tomography) [8], [9]. The usual goal is to characterise how scattering intensity varies vertically, for which useful vertical resolution requires many (ten or more) images acquired on separate passes, which is an impractical collection burden and leads to a difficult phase calibration problem [10]. For the CCD application here, the vertical resolution requirement can be relaxed, permitting fewer image channels, but the full complex 3D output is needed (rare in the SAR literature [11]), so the beamforming method must preserve phase. Fig. 1 depicts a radar system that alternates on transmit between two antennas to acquire three channels in a single pass. Adaptive beamforming (minimum-variance distortionless response (MVDR) [12, ch. 6.2,6.3,6.6] a.k.a. Capon [9]) using this minimal design has been demonstrated by Intermap [13].

Fig. 2 shows the proposed 3D SAR CCD concept. In this work, CCD under a forest canopy is formulated as a multichannel dual-layer coherence estimation problem, and the optimal beamforming solution is derived. The random-volume-over-ground (RVOG) model [14, ch. 5.2.4, 7.2-7.4], used to estimate forest height via model inversion given polarimetric-interferometric SAR (PolInSAR) data [15], is repurposed to analyse the potential performance of a three-channel system.

II. Sensitivity to Change

The complex speckle pattern is the pixel-to-pixel fluctuation in the net coherent response of many scattering elements in distributed clutter [3]. A random rearrangement of scattering elements (e.g. rearranged pebbles on a gravel road) may cause a change in the speckle pattern without changing the overall scattering intensity. CCD aims to detect such subtle changes as decorrelation (coherence loss) between repeat observations [1].

Fig. 3 indicates how shorter wavelengths are more sensitive to subtle scene change. The curves were obtained using a SAR imaging simulation. Sets of raw radar pulse data were synthesised for a homogeneous clutter scene consisting of many randomly distributed point scatterers ($10/\mathrm{m}^2$). For each dataset, the scatterers were randomly (and independently) shifted relative to their original position, giving rise to a different speckle pattern. The shifts were uniformly distributed in angle and normally distributed (with zero mean) in distance. The standard deviation of the distance distribution was changed from dataset to dataset; this is the quantity plotted on the x axis. A SAR image was formed from each dataset and its coherence with the original (zero-shift) image computed (1032 effective looks); this is the quantity plotted on the y axis. To permit comparison across wavelengths, the bandwidth (140 MHz) was fixed to give a constant ground-range resolution (1.7 m), and the aperture lengths were varied to give a constant azimuth resolution (1 m).

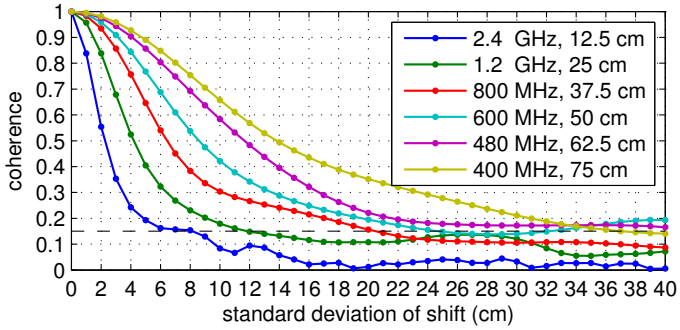

Fig. 3. Coherence magnitude at different wavelengths as a function of the level of change in a clutter scene. Each curve was obtained by repeated execution of a SAR simulation where change was implemented as random shifts in the positions of point scatterers. The resolution was fixed.

For the same change, the decorrelation is greater at shorter wavelengths, even with the resolution held constant. Complete decorrelation (say, coherence 0.15) occurs when the shifts' standard deviation is roughly half of the wavelength. The curves broadly agree with those in [16, Fig.4] for a different simulation.

Given these results, L-band (λ~23cm) is favoured over lower frequencies, despite the better foliage penetration they offer.

III. Multichannel Coherence

Model a pixel in a radar image of clutter as a zero-mean complex random variable x with expected power $\sigma_x^2 = \mathrm{E}\{xx^*\}$.

Given a registered pair of images acquired on repeat passes a and b at grazing angles ψ_a and ψ_b, the complex coherence [3, p. 38] between corresponding pixels x_a and x_b is

$$\gamma_{ab} = \frac{\mathrm{E}\{x_a x_b^*\}}{\sqrt{\mathrm{E}\{x_a x_a^*\}\mathrm{E}\{x_b x_b^*\}}} \approx \frac{\langle x_a x_b^* \rangle}{\sqrt{\langle x_a x_a^* \rangle \langle x_b x_b^* \rangle}} \qquad (1)$$

where the ensemble averages $\mathrm{E}\{...\}$ are implemented as local spatial averages $\langle ... \rangle$ over realisations of the same wide-sense stationary scattering process. The coherence magnitude $0 \le |\gamma_{ab}| \le 1$ quantifies the similarity of the two speckle patterns [1].

Coherence is now reformulated to allow for multiple image channels per pass, combined as a weighted sum.

Consider a set of M registered radar images acquired at grazing angles $\boldsymbol{\psi} = [\psi_1, \psi_2, ..., \psi_M]^T$. Let $\mathbf{x} = [x_1, x_2, ..., x_M]^T$ denote the pixel values at one pixel position. The coherence γ_{ij} between any pair of pixels x_i and x_j is $\gamma_{ij} = \mathrm{E}\{x_i x_j^*\}/\sqrt{\sigma_i^2 \sigma_j^2}$. The covariance matrix is $R = \mathrm{E}\{\mathbf{x}\mathbf{x}^H\} = \left[\mathrm{E}\{x_i x_j^*\}\right] = \left[\sqrt{\sigma_i^2 \sigma_j^2}\, \gamma_{ij}\right]$ for $i, j = 1, 2, ..., M$. In the special case of constant channel power $\sigma^2 = \sigma_i^2 \; \forall i$, $R = \sigma^2 \Gamma$, where $\Gamma = [\gamma_{ij}]$ is a matrix of pair-wise coherences, with $\gamma_{ii} = 1 \; \forall i$.

For a given beamformer $\mathbf{w} = [w_1, w_2, ..., w_M]^T$, the weighted sum is $y = \mathbf{w}^H \mathbf{x}$ with power $\sigma_y^2 = \mathrm{E}\{yy^*\} = \mathbf{w}^H R \mathbf{w}$.

Now consider a repeat-pass pair of multichannel images acquired at grazing angles $\boldsymbol{\psi}_a$ and $\boldsymbol{\psi}_b$. Applying weight vectors $\mathbf{w}_a$ and $\mathbf{w}_b$ to corresponding pixel vectors $\mathbf{x}_a$ and $\mathbf{x}_b$ generates beamformed pixels $y_a = \mathbf{w}_a^H \mathbf{x}_a$ and $y_b = \mathbf{w}_b^H \mathbf{x}_b$ with coherence

$$\gamma_{y_{ab}} = \frac{\mathrm{E}\{y_a y_b^*\}}{\sqrt{\mathrm{E}\{y_a y_a^*\}\mathrm{E}\{y_b y_b^*\}}} = \frac{\mathbf{w}_a^H R_{ab} \mathbf{w}_b}{\sqrt{\mathbf{w}_a^H R_a \mathbf{w}_a \mathbf{w}_b^H R_b \mathbf{w}_b}} \qquad (2)$$

where $R_a = \mathrm{E}\{\mathbf{x}_a \mathbf{x}_a^H\}$, $R_b = \mathrm{E}\{\mathbf{x}_b \mathbf{x}_b^H\}$ and $R_{ab} = \mathrm{E}\{\mathbf{x}_a \mathbf{x}_b^H\}$. The cross-covariance matrix R_{ab} will not be Hermitian.

For repeat-pass change detection, the multichannel grazing angles will typically satisfy the constraints

$$|\psi_{b_i} - \psi_{a_i}| \lesssim 1^\circ \; \forall i \quad \text{and} \quad \Delta\psi_{ij} = \Delta\psi_{a_{ij}} \approx \Delta\psi_{b_{ij}} \; \forall i, j \qquad (3)$$

where $\Delta\psi_{a_{ij}} = \psi_{a_j} - \psi_{a_i}$ within pass a and similarly for pass b.

Given (3), assume that all channels in each (calibrated) multichannel acquisition receive the same power.

$$\left.\begin{array}{l}\sigma_a^2 = \sigma_{a_i}^2 \; \forall i \\ \sigma_b^2 = \sigma_{b_i}^2 \; \forall i\end{array}\right\} \Rightarrow \left.\begin{array}{c} R_a = \sigma_a^2 \Gamma_a \\ R_b = \sigma_b^2 \Gamma_b \\ R_{ab} = \sqrt{\sigma_a^2 \sigma_b^2}\, \Gamma_{ab}\end{array}\right\} \Rightarrow \gamma_{y_{ab}} = \frac{\mathbf{w}_a^H \Gamma_{ab} \mathbf{w}_b}{\sqrt{\mathbf{w}_a^H \Gamma_a \mathbf{w}_a \mathbf{w}_b^H \Gamma_b \mathbf{w}_b}} \qquad (4)$$

Note that $\Gamma_{ab} = \left[\gamma_{a_i b_j}\right]$ contains the coherences across passes.

Furthermore, assume that the two sets of coherences observed in the two passes are the same. This is reasonable if, in addition to (3), the scene does not change dramatically.

$$\Gamma_a \approx \Gamma_b \Rightarrow \left.\begin{array}{c}\Gamma = (\Gamma_a + \Gamma_b)/2 \\ \mathbf{w} = \mathbf{w}_a = \mathbf{w}_b\end{array}\right\} \Rightarrow \gamma_{y_{ab}} \approx \frac{\mathbf{w}^H \Gamma_{ab} \mathbf{w}}{\mathbf{w}^H \Gamma \mathbf{w}} \qquad (5)$$

This multichannel coherence is analogous to that in PolInSAR [14, ch. 6.2.2]; where PolInSAR exploits diversity in polarisation, the 3D processing here relies on diversity in grazing angle.

IV. Dual-layer coherence

Model the forest canopy as a volume containing many scattering elements that together provide a macroscopic scattering response but also permit lossy propagation. Model the ground underneath as a propagation boundary that provides a surface scattering response. This dual-layer structure is shown in Fig. 4.

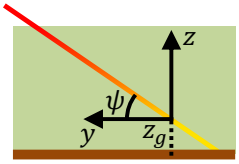

Fig. 4. Dual-layer forest model, consisting of a volume, which is a lossy propagation medium, above a ground surface at $z=z_g$, which is a hard propagation boundary. The model is assumed reasonable at L-band. The SAR images are focused to $z=0$.

Decompose the observed scattering x into independent components g (signal) and v (interference), where g denotes all scattering mechanisms whose interferometric phase centre is located at the ground height, notably direct-surface and ground-trunk double-bounce, and v captures all scattering located above the ground. Modulate g by a (two-way) volume propagation factor p, where $0\le|p|\le 1$. For simplicity, ignore noise and assume that the radar is calibrated perfectly. Hence,

$$x = pg + v, \tag{6}$$

$$\sigma_x^2 = |p|^2\sigma_g^2 + \sigma_v^2 \quad \text{(power } \sigma_q^2 = \mathrm{E}\{qq^*\} \text{ for source } q), \tag{7}$$

$$\mu = |p|^2\sigma_g^2/\sigma_v^2 \quad \text{(effective ground-volume power ratio)}. \tag{8}$$

Given two observations x_a and x_b at ψ_a and ψ_b, split each contributing component into a part that is correlated, c, across the observations, and parts that are uncorrelated, u_a and u_b [16]:

$$\begin{aligned} g_a &= g_c + g_{u_a}, & v_a &= v_c + v_{u_a}, \\ g_b &= g_c + g_{u_b}, & v_b &= v_c + v_{u_b}, \\ \mathrm{E}\{g_a g_b^*\} &= \sigma_{g_c}^2 \mathrm{e}^{\mathrm{j}\phi_g}, & \mathrm{E}\{v_a v_b^*\} &= \sigma_{v_c}^2 \mathrm{e}^{\mathrm{j}\phi_v}, \\ \Rightarrow\ \mathrm{E}\{x_a x_b^*\} &= \mathrm{e}^{\mathrm{j}\phi_g}(p_a p_b^* \sigma_{g_c}^2 + \sigma_{v_c}^2 \mathrm{e}^{\mathrm{j}\phi_{vg}}), \end{aligned} \tag{9}$$

where ϕ_g is the interferometric phase for the ground layer and $\phi_{vg}=\phi_v-\phi_g$ is the interferometric phase for the volume layer relative to the ground. The volume manifests interferometrically as an effective phase centre [17] at height (above the ground)

$$h_{v,\mathrm{eff}} = \phi_{vg}/k_{z0} \tag{10}$$

$$\text{where} \quad k_{z0} = \frac{4\pi}{\lambda}\frac{\Delta\psi}{\cos\psi_0} \qquad \left(\psi_0 = \frac{\psi_a+\psi_b}{2}\right) \quad \text{[2, p. 318]} \tag{11}$$

is the interferometric wavenumber after aperture trimming.

Assume that, across observations, the component powers and the propagation modulation are constant. This is reasonable if, in addition to (3), the scene does not change dramatically.

$$\left.\begin{aligned} \sigma_g^2 &= \sigma_{g_a}^2 = \sigma_{g_b}^2 \\ \sigma_v^2 &= \sigma_{v_a}^2 = \sigma_{v_b}^2 \\ p &= p_a = p_b \end{aligned}\right\} \Rightarrow \begin{aligned} \sigma_x^2 &= \sigma_{x_a}^2 = \sigma_{x_b}^2 = |p|^2\sigma_g^2 + \sigma_v^2 \\ \mathrm{E}\{x_a x_b^*\} &= \mathrm{e}^{\mathrm{j}\phi_g}(|p|^2\sigma_{g_c}^2 + \sigma_{v_c}^2 \mathrm{e}^{\mathrm{j}\phi_{vg}}) \end{aligned} \tag{12}$$

Using (7), (8) and (12), the observed coherence γ_{ab} in (1) is

$$\gamma_{ab} = \mathrm{e}^{\mathrm{j}\phi_g}\frac{|p|^2\sigma_{g_c}^2 + \sigma_{v_c}^2\mathrm{e}^{\mathrm{j}\phi_{vg}}}{|p|^2\sigma_g^2+\sigma_v^2} = \mathrm{e}^{\mathrm{j}\phi_g}\left(\frac{\mu}{1+\mu}\gamma_g + \frac{1}{1+\mu}\gamma_v\right) \tag{13}$$

$$= \mathrm{e}^{\mathrm{j}\phi_g}\frac{\gamma_g+\gamma_v/\mu}{1+1/\mu} \tag{14}$$

where

$$\gamma_g = \sigma_{g_c}^2/\sigma_g^2 \qquad \text{(ground-only coherence; real)} \tag{15}$$

$$\gamma_v = (\sigma_{v_c}^2/\sigma_v^2)\mathrm{e}^{\mathrm{j}\phi_{vg}} \quad \text{(volume-only coherence; complex)}. \tag{16}$$

From (13), ground and volume scattering contribute to the total coherence as a weighted sum, where the weights depend on just the ground-volume power ratio μ. (14) matches (7.38) in [14], except that there it was assumed that $\gamma_g=1$.

The goal is to estimate γ_g, the change parameter for the ground layer. If $|\gamma_{ab}|$ from (13) was used as an estimator for γ_g, then the estimate would be biased by the volume, to the extent determined by μ. If $\gamma_g=1$ (no change), then any decorrelation exhibited by the volume ($|\gamma_v|<1$) would bias the estimate downwards. If $\gamma_g=0$ (complete change), then any correlation exhibited by the volume ($|\gamma_v|>0$) would bias the estimate upwards. Vertically beamforming multiple channels offers a way to increase μ and therefore decrease the volume bias.

V. Multichannel dual-layer coherence

Model the coherence for every channel pair in (4) by the dual-layer expression in (13). For pairs within a pass, the ground coherence will be unity (ignoring noise and assuming aperture trimming [2, ch. 5.2]). Across passes, all pairs observe the same temporal decorrelation (i.e. change); denote the common ground coherence as γ_g. Given (12), μ will be constant for all channels. Given (3) and the weak dependence of k_{z0} on ψ_0, the ground interferometric phases for the pairs within one pass will be approximately equal to the phases for the corresponding pairs within the other pass i.e. $\phi_{g_{ij}} = \phi_{g_{a_{ij}}} \approx \phi_{g_{b_{ij}}}\ \forall i,j$, and similarly for the volume coherences (assuming also that the volume does not change dramatically) i.e. $\gamma_{v_{ij}} = \gamma_{v_{a_{ij}}} \approx \gamma_{v_{b_{ij}}}\ \forall i,j$. Hence,

$$\Gamma = \Gamma_a = \Phi_g \circ \left(\frac{\mu}{1+\mu}\mathbf{1} + \frac{1}{1+\mu}\Gamma_v\right) \approx \Gamma_b, \tag{17}$$

$$\Gamma_{ab} = \Phi_{g_{ab}} \circ \left(\frac{\mu}{1+\mu}\gamma_g\mathbf{1} + \frac{1}{1+\mu}\Gamma_{v_{ab}}\right), \tag{18}$$

where $\Phi_g = \left[\mathrm{e}^{\mathrm{j}\phi_{g_{ij}}}\right]$ is a matrix of ground interferometric phasors for pairs within a pass ($\Phi_{g_{ab}}$ is the same for pairs across passes), Γ_v is a matrix of volume coherences for pairs within a pass ($\Gamma_{v_{ab}}$ is the same for pairs across passes), $\mathbf{1}$ is an $M\times M$ matrix of ones, and $\circ$ indicates the Hadamard product.

Substituting (17) and (18) into (5), the output coherence is

$$\gamma_{y_{ab}} \approx \frac{\mathbf{w}^H\Gamma_{ab}\mathbf{w}}{\mathbf{w}^H\Gamma\mathbf{w}} = \frac{\mu\mathbf{w}^H\Phi_{g_{ab}}\mathbf{w}\gamma_g + \mathbf{w}^H\Phi_{g_{ab}}\circ\Gamma_{v_{ab}}\mathbf{w}}{\mu\mathbf{w}^H\Phi_g\mathbf{w} + \mathbf{w}^H\Phi_g\circ\Gamma_v\mathbf{w}} = \frac{\delta\gamma_g + \beta_v\alpha_v/\mu}{1+\alpha_v/\mu} \tag{19}$$

where

$$\alpha_v = \frac{\mathbf{w}^H\Phi_g\circ\Gamma_v\mathbf{w}}{\mathbf{w}^H\Phi_g\mathbf{w}}, \quad \beta_v = \frac{\mathbf{w}^H\Phi_{g_{ab}}\circ\Gamma_{v_{ab}}\mathbf{w}}{\mathbf{w}^H\Phi_g\circ\Gamma_v\mathbf{w}}, \quad \delta = \frac{\mathbf{w}^H\Phi_{g_{ab}}\mathbf{w}}{\mathbf{w}^H\Phi_g\mathbf{w}}. \tag{20}$$

α_v is a real non-negative number because its constituent matrices are Hermitian positive semi-definite. Moreover, comparing the numerator and denominator matrices, $0\le\alpha_v, |\beta_v|, |\delta|\le 1$.

Compare (19) with (14). The multichannel volume attenuation factor α_v captures the effect of the beamformer $\mathbf{w}$: the effective ground-volume power ratio within a pass is increased from μ to

$$\mu' = \mu/\alpha_v \qquad (0\le\alpha_v\le 1). \tag{21}$$

If the topography of the forested terrain is known (or can be estimated using multichannel/PolInSAR data [13], [15]), then the focal surface for the SAR images can be made to match the true ground surface (the ideal for CCD of the ground), so

$$z_g = 0 \;\Rightarrow\; \phi_{g_{ij}} = 0 \;\forall i,j \;\Rightarrow\; \alpha_v = \frac{\mathbf{w}^H \Gamma_v \mathbf{w}}{\mathbf{w}^H \mathbf{1} \mathbf{w}}. \qquad (22)$$

If the repeat-pass geometries are identical i.e. $\psi_{a_i} = \psi_{b_i} \forall i$ (the ideal for change detection), and the volume is constant, then $\Gamma_{v_{ab}} = \Gamma_v$ and $\beta_v = 1$. If either the collection geometries are identical or the focal and ground surfaces match, then $\delta = 1$.

Consider using $|\gamma_{y_{ab}}|$ from (19) as an estimator for γ_g. In the ideal case $\beta_v = \delta = 1$, the coherence estimation error would be

$$\epsilon_{\gamma_g} = |\gamma_{y_{ab}}| - \gamma_g = \frac{1}{1+\mu/\alpha_v}(1-\gamma_g) = \begin{cases} \dfrac{1}{1+\mu/\alpha_v} & \gamma_g = 0 \\ 0 & \gamma_g = 1 \end{cases} \qquad (23)$$

Limiting the coherence error to, say, 0.1, sets the required α_v:

$$\epsilon_{\gamma_g} < 0.1 \;\Rightarrow\; \alpha_v < \mu/9 \quad (\alpha_v^{(\mathrm{dB})} < \mu^{(\mathrm{dB})} - 9.5\mathrm{dB}). \qquad (24)$$

VI. 3D SAR BEAMFORMING

Scattering elements above or below the focal surface of a SAR image will layover into the image and contribute residual propagation phase; both effects depend on scatterer height and radar grazing angle. Multiple images acquired at different grazing angles will collectively be sensitive to scatterer height via the differential layover and phase. SAR beamforming exploits this by applying a height-selective complex weight vector $\mathbf{w}$ [9]. For CCD, the complex reflectivity of the ground is sought, so only phase-preserving methods are considered.

After accurate motion compensation and removal of flat-earth phase, scatterers on the focal surface will contribute no residual propagation phase. Therefore, the height ($z = 0$) of the focal surface is the SAR-equivalent of the 'broadside direction', for which the steering vector is a vector of ones, denoted $\mathbf{v}_0$.

The gain variation of a beamformer $\mathbf{w}$ is specified by its beampattern $b(z) = |\mathbf{w}^H \mathbf{v}(z)|^2$. In the SAR case, the i^{th} element of the propagation vector $\mathbf{v}(z) = [\mathrm{e}^{\mathrm{j}\phi_i(z)}]$ contains the interferometric phase $\phi_i(z) = k_{z_i} z$ (see (11)) that would be observed if the first and i^{th} channels illuminated a surface at height z.

Two standard types of beamformers are the conventional $\mathbf{w}_{\text{conv}}$ and the adaptive (a.k.a. minimum-variance distortionless response (MVDR) [12, ch. 6.2,6.3,6.6] or Capon [9]) $\mathbf{w}_{\text{mvdr}}$:

$$\mathbf{w}_{\text{conv}} = \frac{1}{N_{ch}} \mathbf{v}_0 \quad (25) \qquad \mathbf{w}_{\text{mvdr}} = \frac{\hat{R}^{-1} \mathbf{v}_0}{\mathbf{v}_0^H \hat{R}^{-1} \mathbf{v}_0}, \quad (26)$$

where the sample covariance matrix $\hat{R}$ requires a spatial average. For approximately uniformly spaced channels, the beampattern of $\mathbf{w}_{\text{conv}}$ will be sinc-like with mainlobe peak-to-null width ρ_z and a grating-lobe ambiguity at h_{amb}:

$$\rho_z = \frac{\lambda}{2M\overline{\Delta\psi}} \cos\overline{\psi} \qquad (27) \qquad h_{\text{amb}} = M\rho_z \qquad (28)$$

where $\overline{\psi}$ is the mean grazing angle and $\overline{\Delta\psi}$ the mean spacing. $\mathbf{w}_{\text{mvdr}}$ optimally minimises the power from all heights without distorting the signal from the steered height; up to $M-1$ nulls are steered onto interferences. Compared to $\mathbf{w}_{\text{conv}}$, $\mathbf{w}_{\text{mvdr}}$ offers improved performance but greater sensitivity to errors [12].

We seek the optimal beamforming weight vector $\mathbf{w}_{\text{opt}}$ that minimises α_v in (22) and thereby maximises μ' in (21).

First note that Γ_v is Hermitian positive semi-definite, since it is a scaled covariance matrix. It will almost certainly be positive definite in practice, so assume that Γ_v^{-1} exists.

Observe from (22) that

$$\frac{1}{\alpha_v} = \frac{\mathbf{w}^H A \mathbf{w}}{\mathbf{w}^H B \mathbf{w}} = \frac{\mathbf{w}^H C C^{-1} A C^{-H} C^H \mathbf{w}}{\mathbf{w}^H C C^H \mathbf{w}} = \frac{\mathbf{w}'^H D \mathbf{w}'}{\mathbf{w}'^H \mathbf{w}'} \qquad (29)$$

where $A = \mathbf{1}$ is Hermitian, $B = \Gamma_v$ is Hermitian positive definite, $B = CC^H$ is the Cholesky factorisation of B [18, pp. 90,441], $D = C^{-1} A C^{-H}$, and $\mathbf{w}' = C^H \mathbf{w}$ is the transformed weight vector. The right-hand side of (29) fits the general form of a Rayleigh quotient, whose bounds are the minimum and maximum eigenvalues of D, achieved when $\mathbf{w}'$ equals the corresponding eigenvectors [18, pp. 234–235]. The eigenvalue problem is

$$D\mathbf{w}' = \lambda \mathbf{w}' \Rightarrow C^{-1} A C^{-H} C^H \mathbf{w} = \lambda C^H \mathbf{w} \Rightarrow E\mathbf{w} = \lambda \mathbf{w} \quad (30)$$

where

$$E = C^{-H} C^{-1} A C^{-H} C^H = (CC^H)^{-1} A (CC^{-1})^H = B^{-1} A. \quad (31)$$

In this case, $E = B^{-1}A = \Gamma_v^{-1}\mathbf{1}$ has unit rank. The only non-trivial eigenvalue $\lambda_{\max} > 0$ and corresponding eigenvector are

$$\lambda_{\max} = \mathbf{v}_0^T \Gamma_v^{-1} \mathbf{v}_0 \qquad \mathbf{w}_{\max} = c\Gamma_v^{-1} \mathbf{v}_0 \qquad (32)$$

for any $c \in \mathbb{C}$ (N.B. $\mathbf{1} = \mathbf{v}_0 \mathbf{v}_0^T$). Hence, the optimal solution is

$$\alpha_{v,\min} = 1/\lambda_{\max} \qquad \mathbf{w}_{\text{opt}} = \mathbf{w}_{\max}/\lambda_{\max} \qquad (33)$$

which matches the usual form for optimal beamforming [12].

Note that $\mathbf{w}_{\text{opt}}$ is optimal for α_v, but not necessarily for $\epsilon_{\gamma_g} = |\gamma_{y_{ab}}| - \gamma_g$, unless $\beta_v = 1$ (requires identical geometries).

VII. RANDOM VOLUME COHERENCE

It would be useful to compare the performance of different radar designs $(M, \overline{\Delta\psi})$ for different model scenes. We use the random-volume-over-ground (RVOG) model, commonly used in PolInSAR for forest height inversion [17], because it has been shown to be widely applicable to different forest types and offers a simple analytical expression for the volume coherence that we can use to populate Γ_v. The canopy is modelled as just a homogeneous random volume of scattering elements extending from the ground to a height h_v. For energy incident at ψ, the two-way penetration length through the volume to the ground and back is $l_p = 2h_v/\sin\psi$. Propagation through the volume in direction ψ is subject to exponential decay, parameterised by an extinction coefficient σ_e (units: m^{-1}). The subsequent two-way attenuation of scattered energy is given by

$$f_v(z') = \mathrm{e}^{-2\sigma_e (h_v - z')/\sin\psi} \qquad (34)$$

where $z' = z - z_g$ is referenced to the ground surface, so $f_v(h_v) = 1$ and $|p|^2 = f_v(0) = \mathrm{e}^{-2\sigma_e h_v/\sin\psi} = \mathrm{e}^{-l_p\sigma_e} > 0$. Figure 5 sketches the effective vertical structure of a random volume.

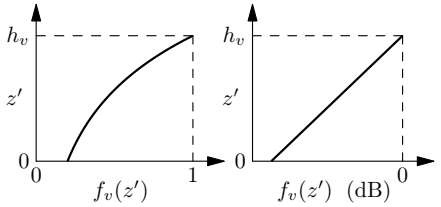

Fig. 5. Effective vertical structure of a random volume with propagation loss given by $f_v(z')$ in (34). The ground is at $z' = 0$.

One aspect that is not clearly explained in the SAR literature (compare to [14, p. 230]) is that the propagation loss can be expressed as a one-way attenuation rate σ_e^{dB} (units: dB/m), which is equivalent to the intuitive concept of cable loss. Given $f_v(0) = \mathrm{e}^{-l_p \sigma_e}$, the decibel loss per unit length in direction ψ is

$$\sigma_e^{\text{dB}} = -\frac{10\log_{10}\mathrm{e}^{-l_p\sigma_e}}{l_p} = (10\log_{10}\mathrm{e})\sigma_e = \frac{10}{\ln 10}\sigma_e. \qquad (35)$$

When observed interferometrically, the coherent superposition of scattering elements from different heights causes volume decorrelation. This is separate from any change in the volume. The random volume coherence is given by [17], [14, ch. 5.2.4.2]

$$\gamma_v = \frac{\mathrm{E}\{v_a v_b^*\}}{\sqrt{\mathrm{E}\{v_a v_a^*\}\mathrm{E}\{v_b v_b^*\}}}\mathrm{e}^{-\mathrm{j}\phi_g} = \frac{p_1(\mathrm{e}^{p_2 h_v} - 1)}{p_2(\mathrm{e}^{p_1 h_v} - 1)} \qquad (36)$$

where $p_1 = 2\sigma_e/\sin\psi$ and $p_2 = p_1 + \mathrm{j}k_{z0}$. Note that γ_v is complex. If $\sigma_e = 0$, then $f_v(z') = 1$, and by L'Hôpital's rule, $\gamma_v = \mathrm{e}^{\mathrm{j}k_{z0}h_v/2}\operatorname{sinc} k_{z0}h_v/2\pi$ (so $h_{v,\text{eff}} = \angle\gamma_v/k_{z0} = h_v/2$), with $\gamma_v = 0$ when $h_{\text{amb}} = 2\pi/k_{z0} = h_v$. As σ_e increases, both $|\gamma_v|$ and $h_{v,\text{eff}}$ increase—the volume tends towards a surface at h_v.

VIII. RVOG Beamformer Performance

Define the RVOG beamformer $\mathbf{w}_{\text{rvog}}$ as the optimal beamformer in (33) obtained when Γ_v is populated with volume coherences predicted by (36) according to the random volume model. Implementation requires estimated or assumed values of the random volume parameters (h_v and σ_e^{dB}) together with the known multichannel collection geometry.

The performance of the RVOG beamformer depends on how closely the modelled volume matches the actual canopy. The assumptions are two-fold: firstly, that the canopy can be well-modelled as a random volume, and secondly, that the canopy is well-modelled by the specified random volume.

Compare $\mathbf{w}_{\text{rvog}} = \Gamma_v^{-1}\mathbf{v}_0$ from (33) with $\mathbf{w}_{\text{mvdr}} = \hat{R}^{-1}\mathbf{v}_0$ in (26), neglecting scale factors. The former is clairvoyant and the latter is data-driven. In cases where it is difficult to obtain a reliable estimate of $\hat{R}$, say due to a limited number of resolution cells to average over, it may be safer to instead employ $\mathbf{w}_{\text{rvog}}$. A mixed approach, whereby the adaptivity is constrained within reasonable RVOG bounds, may be possible.

Fig. 6 shows the best-case performance of the RVOG beamformer for different collection parameters, given a typical RVOG scene. Note that, as the angular spacing $\Delta\psi$ decreases, the optimal performance improves despite the resolution ρ_z in (27) of the conventional beamformer becoming coarser. Even with only three channels, choosing $\Delta\psi{\sim}0.05^\circ$ (matching the Intermap design [13]) would support volume attenuation around $-12\,\text{dB}$, which from (24) is sufficient to permit accurate ground coherence estimates when $\mu > -2.5\text{dB}$ (assuming $z_g = 0$).

The beampatterns in Fig. 7 show how different beamformers suppress the volume. The optimal RVOG beamformer (red) steers two nulls inside the mainlobe of the conventional beamformer (blue), which encompasses the whole volume extent ($h_v = 20\text{m}$ vs $\rho_z = 36\text{m}$). The trade-off for this high performance is large gain for any scattering received from outside the expected scene extent.

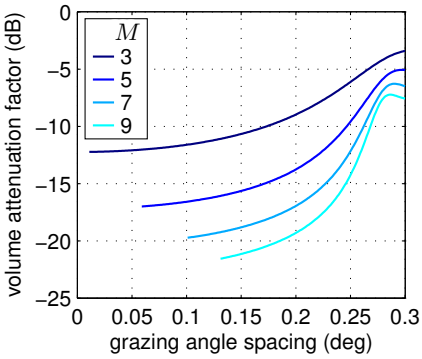

Fig. 6. RVOG beamformer performance: the optimal multichannel volume attenuation factor $\alpha_{v,\text{min}}$ as a function of grazing angle spacing $\Delta\psi$ for different numbers of channels M ($\bar{\psi} = 35^\circ$, $\lambda = 23\text{cm}$). Fixed scene parameters: $h_v = 20\text{m}$, $\sigma_e^{\text{dB}} = 0.1\text{dB/m}$. Each point on each curve was obtained by populating Γ_v with volume coherences from (36) for all channel pairs in the given configuration and then evaluating (33).

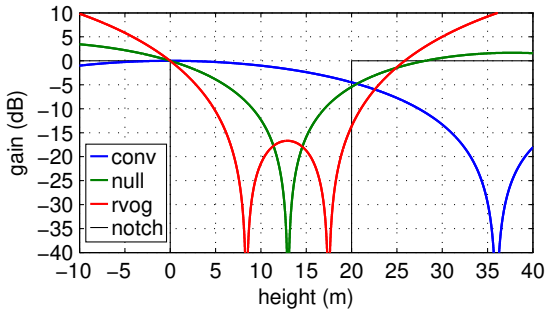

Fig. 7. Vertical beampatterns for conventional ($\alpha_v = -1.8\text{dB}$), null-steer ($\alpha_v = -7.4\text{dB}$) and optimal RVOG ($\alpha_v = -12.1\text{dB}$) beamformers. Collection parameters: $M = 3$, $\Delta\psi = 0.05^\circ$, $\bar{\psi} = 35^\circ$, $\lambda = 23\text{cm}$. Scene parameters: $h_v = 20\text{m}$, $\sigma_e^{\text{dB}} = 0.1\text{dB/m}$. The null-steer beamformer (green) was designed to steer a single null at $h_{v,\text{eff}} \approx 13\text{m}$ (the height of the volume's effective phase centre is slightly different for different channel pairs). The notch lines (black) indicate the ideal filter.

How sensitive is the RVOG beamformer to deviations between the assumed and actual values of the random volume parameters? Fig. 8 shows the ground coherence estimation performance of $\mathbf{w}_{\text{rvog}}$ designed for the collection scenario in Fig. 7 when applied to different random volumes. Broadly, blue (red) indicates good (poor) performance. The black loop marks the acceptable operating region where the estimation error is less than 0.1. The beamformer is moderately sensitive to deviations in the model parameters. Near the design point in this example, the volume height should be known to within about three metres of its true value. Estimating canopy height to this level of accuracy is achievable using PolInSAR [15], [14, ch. 9.5.5].

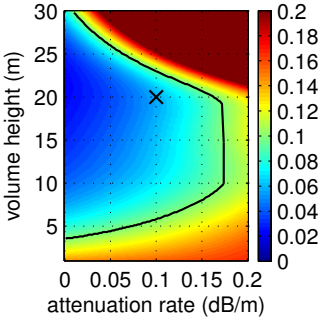

Fig. 8. RVOG beamformer sensitivity: the coherence estimation error ϵ_{γ_g} in (23) for $\gamma_g = 0$ when the RVOG beamformer from Fig. 7 is applied to different random volumes. For each (h_v, σ_e^{dB}) combination, the volume attenuation α_v achieved by $\mathbf{w}_{\text{rvog}}$ was computed via (22) (with Γ_v generated using (36)), and the ground-volume power ratio μ was modified for the new propagation factor $|p|^2 = f_v(0)$ from (34). The black cross indicates the design point: $h_v = 20\text{m}$, $\sigma_e^{\text{dB}} = 0.1\text{dB/m}$, $\mu = 0\text{dB}$. The black line marks the region where $\epsilon_{\gamma_g} < 0.1$.

Note that the random volume parameters determine both the vertical structure for beamforming (captured in α_v) and the propagation loss (captured in μ). For example, as the attenuation rate increases, the volume becomes more localised in height, so

it can be more effectively suppressed by the beamformer, but the propagation loss increases, so the ground signal will be weaker; the latter effect may dominate, as in the top-right of Fig. 8.

IX. Simulation

The 3D SAR CCD concept was tested by simulating RVOG clutter using many point scatterers. Fig. 9 shows the results for a three-channel radar configuration and non-identical passes. For the repeat-pass pair formed by the middle channels only, $\gamma_v = 0.241\angle 339^\circ$ from (36) and $|\gamma_{ab}| = 0.614$ from (14) for $\gamma_g = 1$, which matches the single-channel coherence observed in (c) in the no-change areas. Combining all channels from each pass using the adaptive beamformer, the resulting coherence across passes is $|\gamma_{y_{ab}}| = 0.872$ because the volume, which causes decorrelation, has been suppressed. Thus, the true scene changes on the ground in (a) are visible in the 3D CCD in (e).

X. Conclusion

3D SAR CCD of the ground in a forest would seem to be feasible by applying optimal beamforming techniques to just three across-track image channels. A framework has been established for suitable multichannel radar design and performance analysis using the RVOG model. Of the numerous practical challenges to implementation, obtaining accurate knowledge of the ground height for SAR image formation may be the most difficult.

References

[1] E. J. M. Rignot and J. J. van Zyl, "Change detection techniques for ERS-1 SAR data," *IEEE TGRS*, vol. 31, no. 4, pp. 896–906, Jul. 1993.

[2] C. V. Jakowatz *et al.*, *Spotlight-Mode Synthetic Aperture Radar: A Signal Processing Approach*. Sandia National Laboratories: Springer, 1996.

[3] J. W. Goodman, "Statistical properties of laser speckle patterns," in *Laser Speckle and Related Phenomena*, J. Dainty, Ed. Springer-Verlag, 1975.

[4] M. Preiss, D. A. Gray, and N. J. S. Stacy, "Detecting scene changes using synthetic aperture radar interferometry," *IEEE TGRS*, vol. 44, no. 8, pp. 2041–2054, Sep. 2006.

[5] S. I. Tsunoda *et al.*, "Lynx: A high-resolution synthetic aperture radar," in *Proc. IEEE Aerospace Conf.*, Mar. 2000.

[6] P. B. Pincus, M. Preiss, and D. A. Gray, "3D SAR beamforming under a foliage canopy from a single pass," in *Proc. ICASSP Conf.*, Apr. 2015.

[7] L. A. Bessette and S. Ayasli, "Ultra-wideband P-3 & CARABAS II foliage attenuation and backscatter analysis," in *Proc. IEEE Radar Conf.*, 2001.

[8] C. V. Jakowatz and D. E. Wahl, "Three-dimensional tomographic imaging for foliage penetration using multiple-pass spotlight-mode SAR," in *Proc. Sig., Sys. & Comp. Asilomar Conf.*, Nov. 2001.

[9] F. Lombardini, M. Montanari, and F. Gini, "Reflectivity estimation for multibaseline interferometric radar imaging of layover extended sources," *IEEE TSP*, vol. 51, no. 6, pp. 1508–1519, Jun. 2003.

[10] A. Reigber and A. Moreira, "First demonstration of airborne SAR tomography using multibaseline L-band data," *IEEE TGRS*, vol. 38, no. 5, pp. 2142–2152, Sep. 2000.

[11] M. M. d'Alessandro and S. Tebaldini, "Phenomenology of P-band scattering from a tropical forest through three-dimensional SAR tomography," *IEEE GRS Letters*, vol. 9, no. 3, pp. 442–446, May 2012.

[12] H. L. Van Trees, *Optimum array processing: Part IV of detection, estimation & modulation theory*. John Wiley & Sons, 2002.

[13] Q. Zhang *et al.*, "Forest height estimation using single-pass dual-baseline L-band PolInSAR data," in *Proc. IGARSS*, Jul. 2012.

[14] S. R. Cloude, *Polarisation: Applications in Remote Sensing*. OUP, 2010.

[15] J. Praks *et al.*, "Height estimation of boreal forest: Interferometric model-based inversion at L- and X-band versus HUTSCAT profiling scatterometer," *IEEE GRS Letters*, vol. 4, no. 3, pp. 466–470, Jul. 2007.

[16] H. A. Zebker and J. Villasenor, "Decorrelation in interferometric radar echoes," *IEEE TGRS*, vol. 30, no. 5, pp. 950–959, Sep. 1992.

[17] K. P. Papathanassiou and S. R. Cloude, "Single-baseline polarimetric SAR interferometry," *IEEE TGRS*, vol. 39, no. 11, pp. 2352–2363, Nov. 2001.

[18] R. A. Horn and C. R. Johnson, *Matrix Analysis*, 2nd ed. CUP, 2013.

[19] B. Obama, "G20 speech in Brisbane," *The Courier Mail*, 15 Nov. 2014.

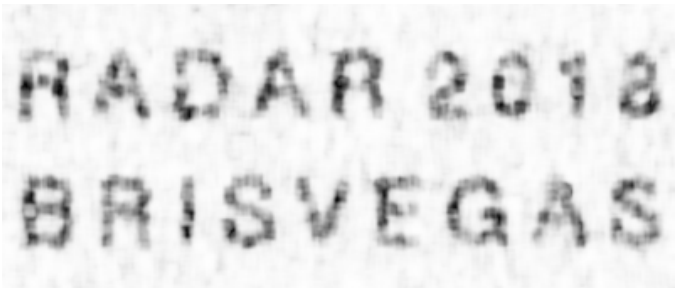

(a) CCD ($|\gamma_{ab}|$) ground-truth (no volume): RADAR2018 BRISVEGAS [19].

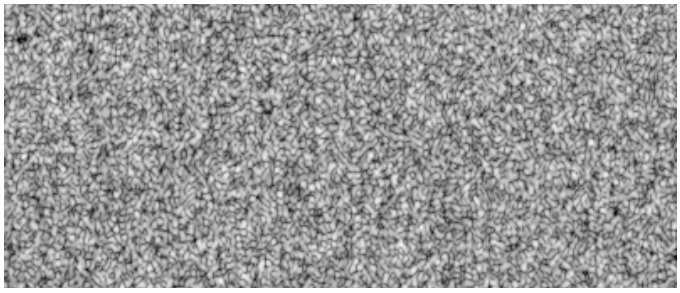

(b) SAR image (dB) of full scene (ground + volume). Consists of speckle only.

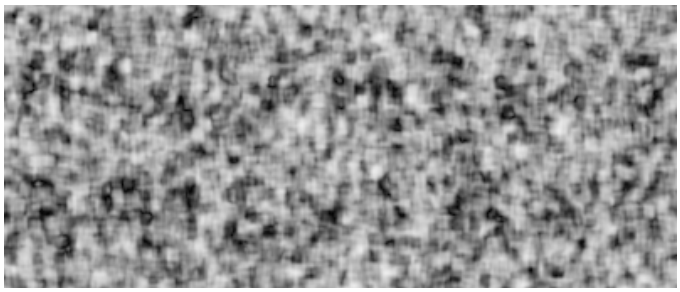

(c) Single-channel CCD of full scene. $\psi_b - \psi_a = 0.3^\circ$, $\overline{|\gamma_{ab}|} = 0.61$

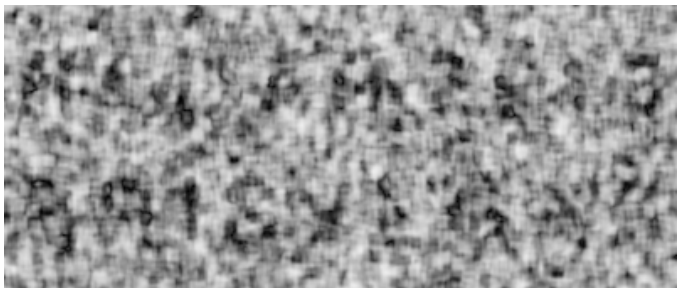

(d) Multichannel CCD using the conventional beamformer. $\overline{|\gamma_{y_{ab}}|} = 0.63$

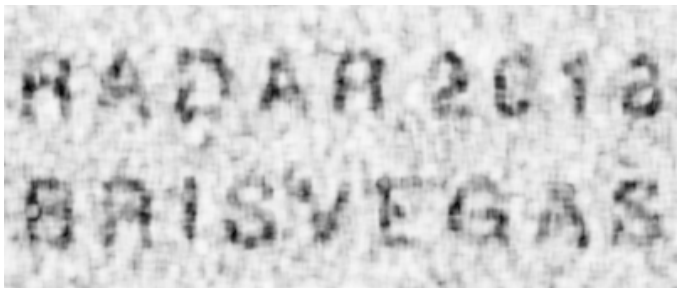

(e) Multichannel CCD using the adaptive MVDR beamformer. $\overline{|\gamma_{y_{ab}}|} = 0.87$

Fig. 9. 3D SAR CCD simulation results. The scene consists of ~2e6 point scatterers that satisfy the RVOG model ($\mu = 0\,\mathrm{dB}$, $h_v = 20\,\mathrm{m}$, $\sigma_e^{\mathrm{dB}} = 0.1\,\mathrm{dB/m}$). Raw echo data were synthesised at L-band ($\lambda = 22.7\,\mathrm{cm}$, $M = 3$, $\Delta\psi = 0.05^\circ$, $\bar{\psi}_a = 35^\circ$, $\bar{\psi}_b = 35.3^\circ$) and focused into SAR images (res. $1\times1.2\,\mathrm{m}$ no window). Between passes, those ground scatterers under a text mask (line-width $1.9\,\mathrm{m}$) were shifted randomly (std deviation $12\,\mathrm{cm}$), causing the decorrelation in (a).